Effect of Poisson's ratio on the indentation of open cell foam

O. Duncan[a*], L. Foster[b], T. Allen[a], A. Alderson[c]

[a] *Department of Engineering, Faculty of Science & Engineering, Manchester Metropolitan University, John Dalton Building, Chester Street, Manchester M15 6BH, UK.*
[b] *Advanced Wellbeing Research Centre, Sheffield Hallam University, Olympic Legacy Park, 2 Old Hall Rd, Sheffield S9 3TU.*
[c] *Materials and Engineering Research Institute, Sheffield Hallam University, Howard Street, Sheffield S1 1WB UK.*
***** Corresponding author (Email: O.Duncan@mmu.ac.uk)

Abstract

We tested whether conventional and auxetic (negative Poisson's ratio) foam indentation response fits with classical indentation theory. We first made foam cubes with 20 to 25 mm sides, and Poisson's ratios spanning negative and positive values (-0.35 to 0.3). These foam cubes were compression tested, and indented by the curved face of two cylinders (10 and 50 mm diameters) and a stud (12 mm diameter), to 20% of their thickness. Full-field true strains were measured by digital image correlation, to obtain Poisson's ratios and to study foam deformation during indentation. Indentation force vs. displacement was measured and calculated using incremental Poisson's ratios and tangent moduli. Normalised root mean square errors between measured and calculated indentation forces were ~5% of measured values. Foam densification during indentation, and compression towards sample edges, increased with the magnitude of negative Poisson's ratio; these may both increase indentation resistance beyond predictions from indentation theory.

Keywords

Indentation and Hardness, Contact Mechanics, Mechanical Testing, Foam Material, Digital Image Correlation

1. Introduction

Auxetic materials with their negative Poisson's ratio (NPR) have some enhanced or extreme characteristics [1,2], which are covered in various textbooks and reviews (e.g., [3–11] . Indentation resistance, or hardness (H), is the pressure required to compress an elastic half-space with an indenter, such as a sphere or flat ended cylinder (radius R), to a specific depth (h) [12]. Considering contact incidence (summarised by x), contact area (A), and force (F), the indentation resistance of an isotropic material is related to Poisson's ratio (ν) and Young's modulus (E), by [12–14]:

$$H = {}^{F}/_{A} \propto \left(\frac{E}{(1-\upsilon^2)}\right)^{x} \quad \textbf{(1)}$$

Indentation hardness has the dimensions of pressure. So, it may be argued that Equation 1 provides exact solutions when x is 1 [15], but has been applied to approximate for other indenters (e.g. a sphere, with x = 2/3 [13]). According to Equation 1, the maximum indentation resistance of isotropic materials of a given Young's modulus occurs when Poisson's ratio is -1. For indentation with a flat ended cylinder (referred to herein as a stud), x is expected to be 1 [13,16], and indentation force is [17–19]:

$$F = 2Rh\frac{E}{(1-\nu^2)} \quad \textbf{(2)}$$

Considering indentation by the curved face of a cylinder (referred to herein as a bar), contact force can be approximated as [18,19]:

$$F \approx \frac{\pi}{4} lh\frac{E}{(1-\nu^2)} \quad \textbf{(3)}$$

whereby l is the length of contact. Note the bar's radius is not in Equation 3, meaning contact area is unknown, so Equation 3 should always be verified or validated before use [20].

Equations 1 to 3, and others describing Hertzian indentations [12], have four key assumptions: i) The surfaces are continuous and have non-conforming profiles; ii) the area of contact is much smaller than the contacting bodies; iii) the strains are small and purely elastic; iv) the contacting surfaces are frictionless. In assumptions ii) and iii), "small" is not defined.

Open cell [2,21,30–32,22–29] auxetic foams are well suited to test theory (like Equations 1 to 3), as we have good knowledge of how to make them [21–27], particularly thermo-mechanically [2,28–32]. Such thermo-mechanical fabrications use a tri-axial volumetric compression ratio (VCR, original/compressed volume) to buckle foam cell ribs [2,28–32], which are then fixed over time by heating and cooling. These fabrications increase foam density, change Young's modulus, and can remove the tendency for open cell foam to undergo plateauing of the stress vs. strain response as cell ribs buckle (typically beyond ~5 to 10% compression) [2,29,30,33].

The effect of NPR on indentation theory has been broadly shown when comparing auxetic and conventional (positive Poisson's ratio) open cell foam [34–36], microporous polyethylene [13,37], and through Finite Element Analysis (FEA) [38–41]. Auxetic foam [34–36] and microporous polyethylene [13] had higher indentation resistance than their conventional counterparts. Agreement with indentation theory (Equation 1) for tests of microporous polyethylene was shown at low indentation loads [13]. In a comparative indentation test, an auxetic foam ($\nu = \sim -0.7$) had over three times higher normalised indentation force (F/E) than a zero Poisson's ratio one [35].

Some analysis of auxetic and conventional foam has also considered characteristics beyond Hertzian indentation theory. Increasing friction between a sample and indenter is thought to increase the effect of Poisson's ratio on indentation resistance [39,42]. Auxetic foam can conform around an indenter [43], increasing the effect of friction, or compress more evenly than conventional foam (and by more overall) around an indenter [35,38–41,44]. These examples appear to differ, with auxetic foam either conforming around an indenter or remaining flat. To attribute the conforming profile of the foam purely to NPR does not reflect differing Young's (and so shear) modulus between auxetic and unconverted foam samples.

A detailed confirmation of the specific effects of NPR, by direct comparison to indentation theory (Equations 1 and 2), remains largely unresolved. Here, we create and test the fit of discrete (strain dependent) models (from Equations 2 and 3) using quasi-linear isotropic foams with Poisson's ratios between -0.35 and 0, and non-linear, anisotropic unconverted foams Poisson's ratios of ~0.4 [28,45]. Vector mapping of surface deformation and full-field strain measurements quantify further potential benefits of NPR, including densification [36] and changes to the upper surface profile [35,43,46].

2. Methods

2.1. Sample fabrication

Open cell foam samples (PUR30FR, Custom-foams, 32 × 32 × 96 mm, cut by the supplier) were thermo-mechanically converted using a process used before [28]. Conditions (VCRs of 2.2 to 5.0) were selected to give a range of negative (~-0.35) to near zero Poisson's ratios, and quasi-linear stress vs. strain relationships [28,47]. Isotropic compression in metal moulds with tri-axial VCRs of 2.2, 3.0 or 5.0 was followed by heating in an oven (MCP Tooling Technologies LC/CD), at; 160 °C for 20 minutes (VCR = 5.0), 160, 170 or 180 °C for 20 minutes, 180 °C for 60 minutes (VCR = 3.0) or 180 °C for 60 minutes (VCR = 2.2).

Six foam samples were fabricated for each time, temperature and VCR combination, then cooled to room temperature in their moulds (30 to 60 minutes). Fabrication, storage and testing was in air-conditioned rooms with temperatures of ~20 to 25 °C and relative humidity of ~30 to 60%, close to the ~23 ± 2 °C and 50 ± 5% in ASTM D3574 − 11 [48]. After cooling, residual stresses were removed by manually stretching the foam samples [26,28,29] to ~10% strain for five cycles at about five seconds per cycle, during which they partially expanded. Fabricated samples were laser cut into 20.5 to 25.5 mm sided cubes (Trotec 10000) the day after fabrication, making two cuts perpendicular to sample length. The central cube cut from each converted foam sample was used for compression and indentation testing. Comparative

unconverted ~20.5 mm sided foam cubes were included, laser cut from the 32 × 32 × 96 mm cuboids.

2.2. Mechanical testing

Compression (flat plate) and indentation tests (**Figure 1**) began two days after fabrication and took a week to complete, for each group of samples. The standard for indentation testing foams (ASTM D3574 − 11 [48]) specifies a cylindrical flat punch indenter, with a diameter (200 mm) about half that of the foam samples (380 × 380 × 100 mm). Sample dimensions were smaller than those stated in ASTM D3574 − 11, as is common in this type of work [25,30,36,49], as large auxetic foam samples are prone to manufacturing imperfections [29,49–51]. So, to maintain relative indenter to sample size, smaller indenters than in the standard were used.

Tests were on an Instron 3367 with a 500 N load cell, sampling at 25 Hz, with an applied strain rate (or equivalent) of 0.0067 s^{-1} and a preload of 0.04 $\pm$ 0.01 N. Tests were filmed (Nikon D810, 28–300mm lens, 1,920 × 1,080 p, 25 fps) for full-field engineering strain measurement by two-dimensional digital image correlation (DIC, GOM Correlate 2016). Indentation to 20% of sample thickness parallel to the z-axis, with recorded transverse deformation along the y-axis, was undertaken (Figure 1). Three indenters were used; the curved face of 10 and 50 mm diameter bars and the end of a 12 mm diameter metal football stud (a scaled down version of the test in ASTM D3574 − 11 [48]). Tests to 20% compression in the same orientation as the indentation tests were undertaken before and after each indentation test, to obtain incremental Young's modulus and Poisson's ratio to apply to Equations 1 to 3. Compression tests to 10% compression in the x- and y- axis and measured transverse engineering strain along the z- or x-axis (respectively), were also done at the start and end of the study, to confirm isotropy or account for anisotropy in the analysis.

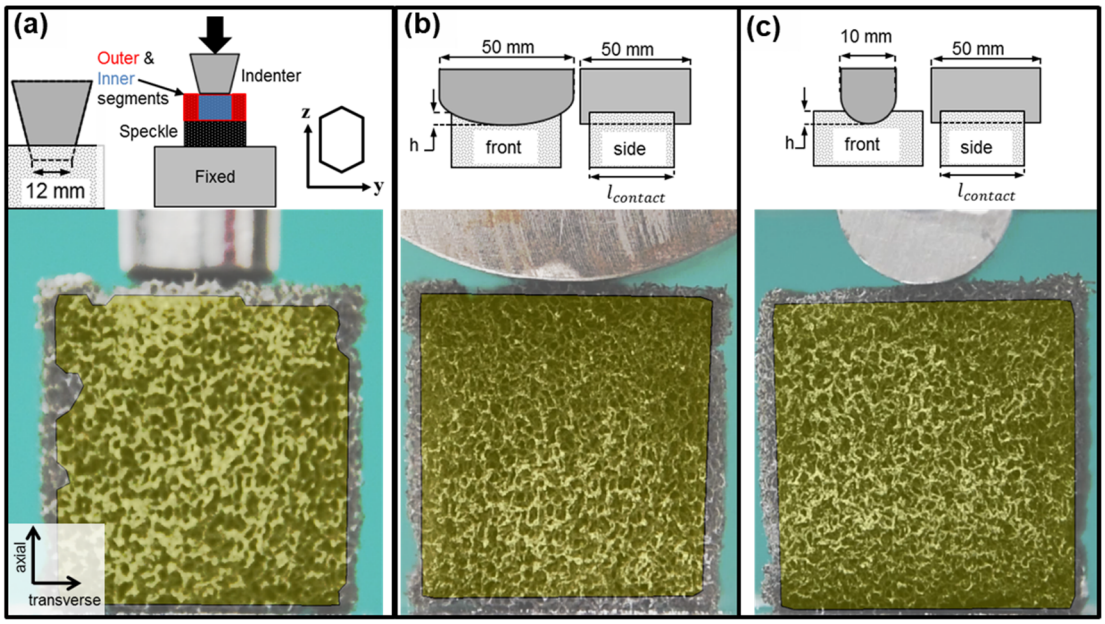

Figure 1: Indentation test set up, including speckle pattern and target area (yellow) for DIC, and schematics showing indenter dimensions, for a) 12 mm studded, b) 50 mm cylindrical & c) 10 mm cylindrical indenters. Additional schematics in (a) show segmentation, used to calculate the ratio of outer/inner compression during indentation, and axis naming of unconverted foam in relation to cell rise.

Axial and transverse engineering strains were obtained by DIC [50,52,53] during indentation and compression tests, then converted to true strain ($\varepsilon_t = \ln(1+\varepsilon_e)$). Powder coating (Laponite RD, BYKAdditives) was applied to the front face of each sample (Figure 1) to enhance the speckle pattern provided by the porous foam surface [28]. DIC facet sizes were between 25 and 35 pixels (0.04 to 0.06 mm/pixel), standard accuracy (max intersection deviation = 0.3 pixels and minimum pattern quality = 1.1) and matching against the previous stage (due to the large strain range) were selected. All samples were measured (Vernier Callipers) before each test (i.e., thirteen times each), to calculate engineering stress and strain from force and displacement data from the uniaxial test device (Bluehill 4.0, Instron, Massachusetts, USA), and final volume ratio (FVR, original/final volume). Note that FVR is often different to VCR, as FVR includes any volume change that can happen after fabrication [28].

Straight lines fitted to transverse vs. axial true strain data were used to obtain Poisson's ratios (the product of -1 and the trend line slope) in all three orthogonal planes (ν_{xz}, ν_{yx}, ν_{zy}). Young's moduli were calculated similarly from the test device true stress and strain data. The

cross sectional area for true stress was corrected according to incremental transverse strain, assuming samples were transversely isotropic. Tangent moduli and Poisson's ratio were calculated at 5 and 10% engineering strain increments for each sample, and are shown to 10% strain, with the 5% increments used in the indentation analysis.

2.3. Indentation Analysis

To test fit between Equations 2 or 3 and experimental data, incremental tangent moduli (E_z) and Poisson's ratios (ν_{zx}) were calculated over 5% applied true strain increments. Incremental force constants ($k_i = \Delta F/\Delta h$) were calculated from Equations 2 and 3, and used to calculate incremental forces (F_i):

$$F_i = F_{i-1} + \frac{k_i \Delta h}{2} \quad \textbf{(4)}$$

whereby h_i = 2.5% of foam thickness, Δh spans h_{i-1} to h_{i+1} and $F_0 = h_0 = 0$.

For the small bar (R = 5 mm), indentation depth (h ≈ 4 mm) was only slightly smaller than indenter radius. Assumptions such as the contact radius being approximately $\sqrt{2Rh}$ (e.g., as described by Popov [17]) would not apply. As approximate solutions for such large relative depth cylindrical indentations diverge, Equation 3 was replaced with an asymptotic equation derived by Argatov *et al*., [54].

$$\frac{h}{h_0} = \frac{F}{F_0}\left\{ln\frac{F_0}{F} - D_0 - D_1\frac{F}{F_0} - D_2\left(\frac{F}{F_0}\right)^2 - D_3\left(\frac{F}{F_0}\right)^3\right\} \quad \textbf{(5)}$$

with the notation:

$$F_0 = \frac{\pi E^* l t^2}{4R}, h_0 = \frac{t^2}{4R}, D_0 = 2d_0 - 2ln2, \quad \textbf{(6)}$$

$$D_1 = \frac{3d_1}{2}, D_2 = {d_1}^2 + \frac{5d_2}{2}, D_3 = \frac{175}{32}d_3 + \frac{25d_1}{4}d_1 d_2 + \frac{5d_2}{6}{d_3}^3 \quad \textbf{(7)}$$

whereby t is foam thickness, E^* is effective modulus ($E/(1-\nu^2)$ for isotropic elastic materials), and d_0 to d_3 are constants that are independent of elastic properties (d_0 = 0.3517, d_1 = -0.521, d_2 = 0.1349, and d_3 = 0.0346 [54]). We solve for F numerically, by iterating values for F

between 0 and a value larger than any of those in the experiments (150 N) in 0.001 N increments. We then used the converged minimum magnitude of the difference between the left and right hand sides of Equation 5. As the unconverted samples were expected to be anisotropic (with transverse isotropy) [28], the effective modulus (for all indenters) was corrected – based on examples presented by Popov [55]:

$$E^* = \frac{2\sqrt{G_{yz}} \times (E_y E_z - (\nu_{zy} E_y)^2)}{\sqrt{E_y} \times \sqrt{(\sqrt{E_y E_z} + \nu_{zy} E_z) \times (\nu_{zy} E_z + 2G_{yz} + \sqrt{E_y E_z})}} \quad \textbf{(8)}$$

Incremental values were used for axial E_z and ν_{zy}, as with analysis of other samples. Transverse strains were assumed to be small (<5%), so constant E_y and ν_{yz} measured up to 5% compression were used. Shear modulus (G_{yz}) was calculated from compression test data, based on Huber's geometric averaging method [56,57]:

$$G_{yz} = \frac{\sqrt{E_y E_z}}{2(1+\sqrt{\nu_{yz}\nu_{zy}})} \quad \textbf{(9)}$$

To account for differences in stiffness between samples, indentation force was normalised to mean Young's moduli (E_z), measured up to 5% true strain before and after each indentation [35]. Mean predicted and measured indentation forces for each group of samples, at each 2.5% increment, were calculated. Normalised root mean square errors (NRMSE) assessed model fit, based on the observed unbiased distribution of the differences between measured (F_m) and calculated (F_c) forces [58]:

$$NRMSE = \frac{\sqrt{\frac{1}{n}\sum(F_m - F_c)^2}}{Max\ F_m} \quad \textbf{(10)}$$

for the n = 7 data points comprising F_c and F_m data at the same indentation depths.

2.4. Indentation strain mapping

Vector plots of virtual facets placed manually in a grid (5 × 4) on foam samples showed localised material deformation during indentation. To show whether observations from vector plots were reliably seen, strain mapping during indentation was applied to samples with ~25.5

mm sides, but different expected Poisson's ratios of -0.2 and zero [28]. Firstly, pseudo Poisson's ratios (from the indentation tests) were measured from straight lines fitted to mean axial and transverse true strains (DIC, Figure 1), up to maximum indentation depth (named pseudo Poisson's ratios because these are not determined from strict uniaxial loading in the indentation tests and so these are not true Poisson's ratio measures). Agreement between pseudo and true Poisson's ratios (from the compression tests) were assessed using a Bland-Altman analysis [59,60].

Central and edgewise axial compression was also compared during indentation tests to determined how uniform axial compression was across sample faces. Faces were split into three segments in the DIC software, reaching to half sample thickness: an inner 10 mm wide segment and two outer segments, each ~7 mm wide (Figure 1a). The ratios of mean axial compression in the two outer segments to those of the inner segment were calculated, with a higher ratio (i.e., closer to 1) corresponding to more even compression, and hence more overall compression. A between group's student's T-test (z = mean difference/pooled standard deviation, with six samples per group) was used to show the effect size between each group and indenter. The probability of falsely rejecting the null hypothesis, wrongly concluding that auxetic and zero Poisson's ratio foams had different ratios of outer to inner compression, was set at 5% ($z > 1.96$, $p < 0.05$ [61]).

3. Results

3.1. Characterisation

Mean final volume ratios FVRs through the course of testing (Figure 2**a**) were close to the imparted VCRs for most samples. Samples fabricated at 160 °C for 20 minutes partially expanded to give a mean FVR of 2.2 (VCR = 3.0) or 3.3 (VCR = 5.0), as intended [28]. The honeycomb-like structure of the unconverted foam (Figure 2b) became quasi-re-entrant and contorted following conversion (Figure 2c). There was no noticeable difference to cell structure

nor shape following prolonged heating (Figure 2d). As expected [2,28,62], cell rise (Figure 2b) was not evident after the re-entrant structure was adopted (Figure 2c & d).

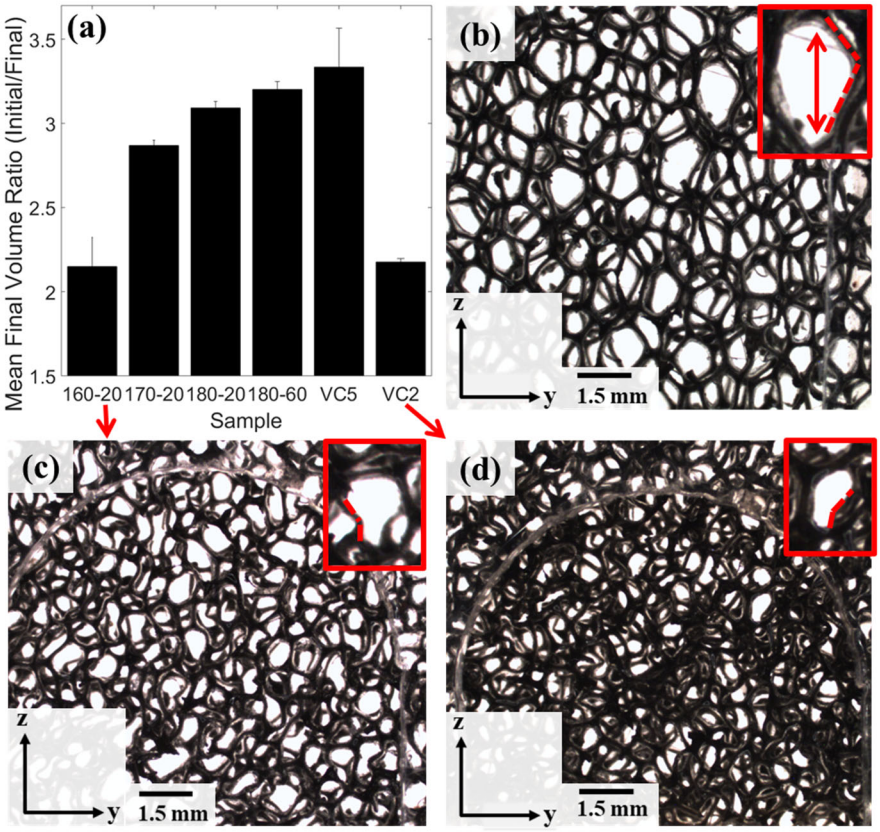

Figure 2: a) Mean Final Volume Ratio (all samples). Error bars show 1 standard deviation. X-axis naming is conversion temperature (before dash, °C) and time (minutes), for all samples fabricated with VCR=3. VC2 were 180 °C, 60 minutes with VCR=2.2, VC5 were 160 °C, 20 minutes with VCR = 5. b) to d) Magnified images (Leica S6D) of 1 mm thick slices of b) unconverted foam, c) auxetic foam (160 °C-20 in (a)), d) ~zero Poisson's ratio foam (VC2 in (a)). Annotated inserts show a cell enlarged by a factor of two, cell rise in b), and identify positive or negative rib angles.

Transverse vs. axial true strain, and true stress vs. strain relationships, were quasi-linear; other than the unconverted foam which plateaued beyond ~5% compression (**Figure 3**). Poisson's ratios were as expected based on prior work [28,49]. Converted samples were approximately isotropic (within one standard deviation), with Poisson's ratios from ~-0.35 to ~0 (Figure 4a). The lowest Poisson's ratios (~-0.35) were achieved following re-expansion from a VCR of 5.0 to an FVR of 3.3. Unconverted samples had anisotropic and positive Poisson's ratios of ~0.25 or ~0.35 when compression was perpendicular or parallel to cell rise

(z), respectively (Figure 4a). Unconverted foam's Poisson's ratios were higher (~0.50) when measured up to 5% rather than 10% compression (Figure 4a), as expected (Figure 3c).

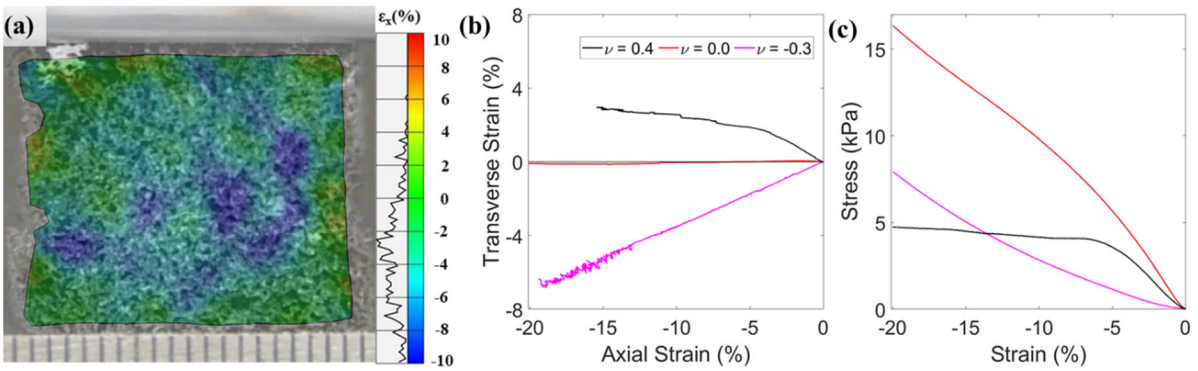

Figure 3: a) Contour plot showing transverse engineering strain for an auxetic (VCR = 5, 160 °C, 20 minute, sample) at 20% compression; b) transverse vs. axial true strain (select samples including iso-density auxetic and near zero Poisson's ratio samples); c) true stress vs. strain (same samples and legend as (b)).

Young's moduli of converted samples were also approximately isotropic, and increased from 20 to 100 kPa with increasing heat exposure (Figure 4b). Unconverted samples had a Young's modulus (to 10%) close to the lowest values for converted samples (~40 kPa, Figure 4b), as expected [46]. The Young's moduli of unconverted foam up to 5% compression were 60 to 80 kPa depending on the orientation (Figure 4b), again, as expected [28].

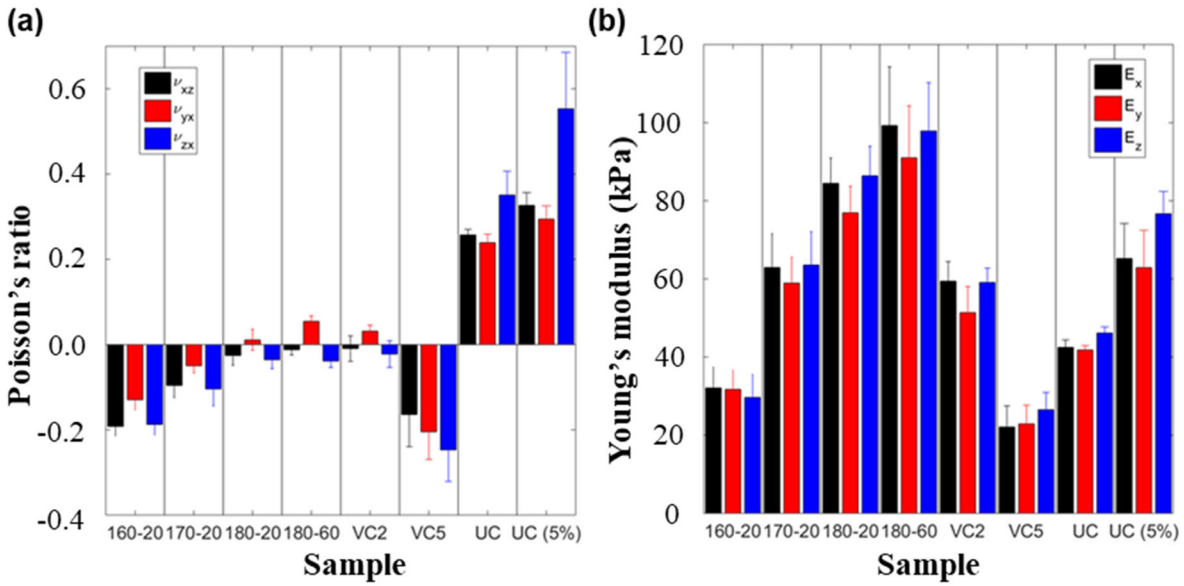

Figure 4: a) Poisson's ratios and b) Young's Moduli taken up to 10% axial for all samples, and also 5% for the unconverted foam. X-axis naming is conversion temperature (before dash, °C) then time (minutes), for all samples fabricated with VCR = 3. The 'VC2' samples were heated for 60 minutes at 180 °C for VCR = 2.2, 'VC5' were heated for 20 minutes at 160 °C for VCR = 5. UC is unconverted. Error bars are 1 standard deviation.

3.2. Indentation resistance

The gradient of normalised indentation force vs. depth increased as Poisson's ratio decreased to negative values (Figure 5), corresponding to an increase in indentation resistance. The indentation force vs. displacement relationships for the unconverted samples (black line, $\nu \approx 0.4$) tended to straighten as the indenter size reduced from the 50 mm to the 10 mm bar (Figure 5b, a then c), suggesting the onset of the buckling region became less sudden.

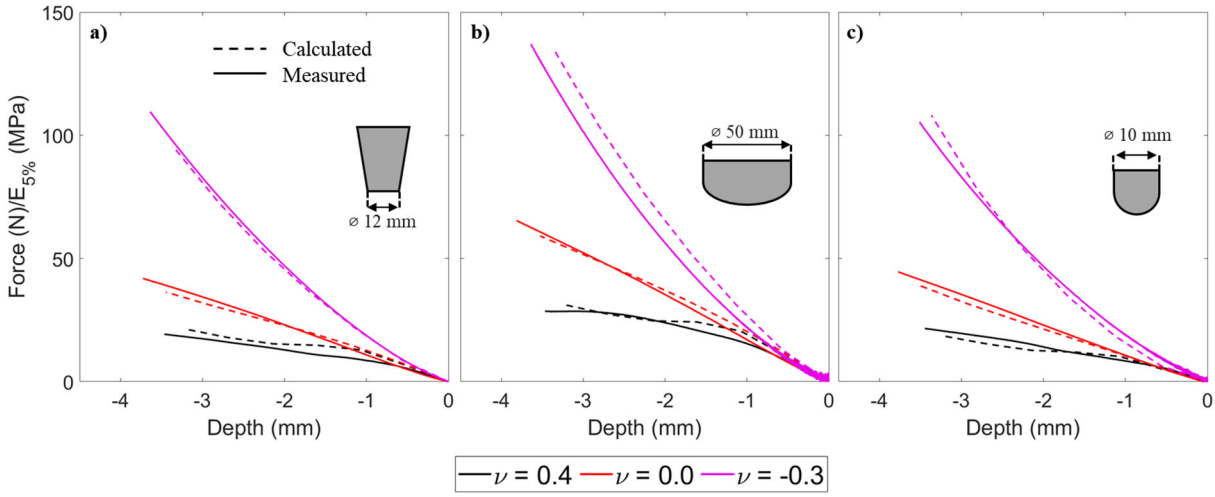

Figure 5: Indentation force, normalised to Young's modulus measured up to 5% true strain, vs. indentation depth for the a) 12 mm stud, b) 50 mm bar and c) 10 mm bar. All data are the mean of the six samples in each group. Calculated indentation forces were based on Equation 4, and a) Equation 2; b) Equation 3; c) Equation 5. Unconverted samples effective modulus (E*) was from Equation 8 (with E_y = 70 kPa and ν_{yz} = 0.3, from Figure 4). The ν = 0.4 group was labelled unconverted, ν = 0.0 was 180-20 and ν = -0.3 was VC5 in Figure 1. Supplementary Figure S1 is a similar plot showing all seven sample groups.

Normalised RMSEs between measured and calculated data were ~5% of maximum values (Table 1), meaning 95% of data would be expected to fall within 10% of the predicted values [58]. Using standard analysis, rather than Equations 5 and 8, NRMSEs were ~40% for indentations with the 10 mm bar and for the unconverted samples.

Table 1: Normalised RMSEs (Equation 10) (in %) between calculated and measured indentation forces

Group	ø12 mm Stud	ø50 mm Bar	ø10 mm Bar
UC	14	8	6
160-20	3	9	6
VC2	4	8	6
170-20	5	4	2
180-20	4	4	3
180-60	4	3	1
VC5	2	7	9
Combined	**5**	**6**	**5**

3.3. Indentation strain mapping

Vector plots (**Figure 6**a to c) show auxetic foam (ν ≈ -0.3) contracted transversely underneath each indenter. Compression was higher underneath the indenters than towards the edge of samples (5 to 15%, Figure 6a and c). Compression (measured at the outer surface) was also lower than the applied depth of 20% on the face for the studded indenter (5 to 10%, Figure 6b), which directly contacted the centre of the sample. Vector plots of indentation with the 10 mm bar show a clear difference between outer and inner foam regions (Figure 6c to e). Auxetic foam (ν ≈ -0.3 Figure 6c) compressed more (by up to 10%) towards its edges than the zero and positive Poisson's ratio samples (~5%) (Figures 6d & e). Both the near zero and NPR samples retained their respective low or inward transverse strain during indentation (Figure 3b, Figures 6c & d), while the unconverted foam expanded (Figures 6e). The same trends were apparent for all indenters (see supplementary materials, and video).

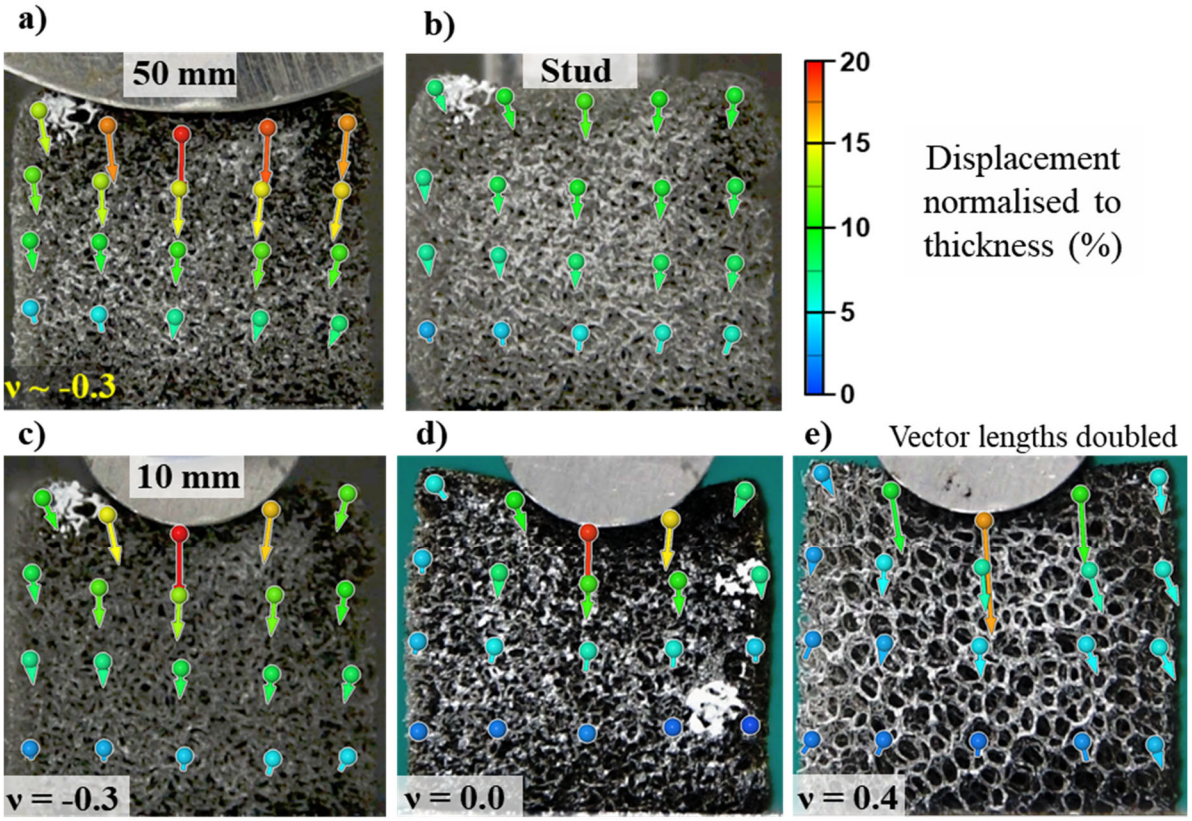

Figure 6: Vector plots of deformation at maximum indentation depth (percentage of sample thickness), a) to c) for an auxetic foam (ν = -0.3), by; a) the 50 mm bar, b) the 12 mm stud, and c) the 10 mm bar. d) Zero Poisson's ratio and e) the unconverted samples at maximum indentation by the 10 mm bar. Due to low deformation, vector lengths in (e) were doubled so they can be seen. Same legend b) for all.

Compressive and indentation pseudo-Poisson's ratios of near zero and NPR samples were similar, with a mean difference of less than -0.01 and limits of agreement between -0.04 and +0.03 (Figure 7a). Differences in the ratio of the outer to inner axial compression were not seen for indentation tests with the 50 mm bar (Figure 7b), which as the largest indenter was more like a flat plate (Figure 6a). The ratio of outer to inner compression was higher ($p < 0.05$) for NPR than zero Poisson's ratio samples during indentation with the 10 mm bar ($z = 1.98$, $p = 0.05$, Figure 7b), and the stud ($z = 2.18$, $p = 0.03$, Figure 7b).

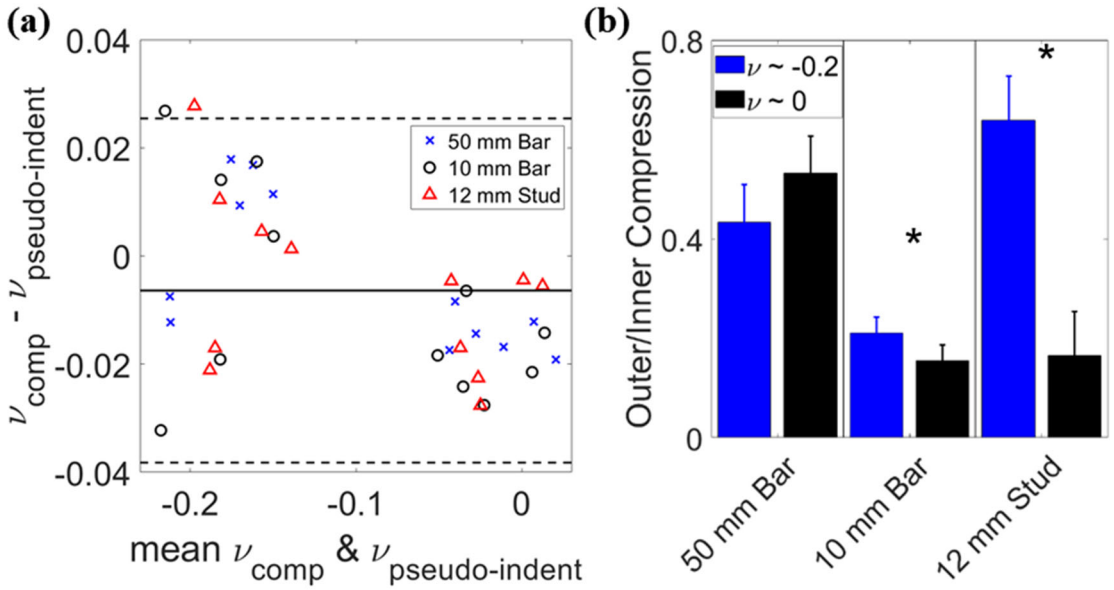

Figure 7: a) Bland Altman plot showing levels of agreement between pseudo Poisson's ratio ($\nu_{pseudo\text{-}indent}$) measured during indentation, and Poisson's ratio measured by compression (ν_{comp}), for two groups with the same dimensions but different Poisson's ratios (160 °C, 20 minutes, VCR = 3 and 180 °C, 60 minutes, VCR = 2.2). b) The ratio of outer/inner compression (Figure 1), for the same group as in (e), at maximum indentation depth for each indenter. Error bars show 1 S.D., * indicates significant differences ($p < 0.05$).

4. Discussion

Auxetic foam samples (with Poisson's ratios of -0.3) exhibited the highest normalised indentation force (F/E, Figure 5). The increased normalised force was attributed to the higher magnitude of tangent modulus and Poisson's ratio (Figure 4), sustained to a higher applied strain (Figure 3), and was expected based on Equations 1 to 3. Indeed, we found close fit (NRMSE ~5%) between measured indentation forces and theoretical values (Figure 5, Table 1). Alternative equations capable of obtaining force at high indentation depths, relative to

indenter radius (Equation 5), and anisotropy in unconverted samples (Equation 8), reduced errors by a factor of ~8 (from ~40% to 5%).

The approximate solution provided by Equation 3 agreed with the data here (Figure 5b). For similar indentations where Equation 3 does not fit, exact solutions are available [63]. Application of Equation 5 would be unsuitable when using the large indenter, with contact width approaching sample thickness [54]. For application of Equations 5, sample thickness should ideally be smaller than contact length (l), to assume an even 2D stress state [54]. With the similar thickness and length here, and relatively low magnitude Poisson's ratios, the change in plane stress at sample outer faces ($\propto E/(1-\nu^2)$ [63]) caused relatively low errors (Figure 5c).

Deviation between calculated and measured forces were highest for the unconverted foams (Table 1), around the onset of foam cell rib buckling (~1 mm indentation depth, Figure 5). Buckling was less pronounced during indentation (Figure 5) than in compression (Figure 3), possibly due to the deforming cells being localised under the indenter, and hence there being fewer buckling cells. The calculated forces did not reflect the less pronounced buckling, despite measurement of properties across the buckling region (i.e., increment i=2 at 5% of sample thickness, using moduli measured between 2.5 and 7.5% compressive strain). In Figures 6e (and supplementary Figure S2a), the front face of the unconverted foam deforms due to buckling of cell ribs close to the indenter, while both converted foams (Figures 6c & d) show a continuous deformation gradient through their thickness. These calculated, and visible, differences suggest that the relatively low number of unconverted foam cells contacting the indenter deform differently during compression and indentation. Micropolar methods have better reflected the bending of foams with few cells than the classical approach used here [64], and could be applied to foam indentations in future work.

Strain vector mapping and full-field strain measurements support claims of extra potential benefits of auxetic materials to cushioning (including seating, packaging and

protective devices) [35,38–41,65,66]. Vector plots (Figure 6a to c) and pseudo Poisson's ratios during indentation (Figure 7a) show auxetic foam contracted transversely during indentation. Density would, therefore, increase more during indentation of auxetic samples than for those with a positive Poisson's ratio that expanded transversely (Figure 6d & e), which may increase indentation resistance as foam ribs touch at higher indentation depths.

Samples with a lower Poisson's ratio (NPR < zero Poisson's ratio < positive Poisson's ratio) deformed more away from the indented area, with a 'flatter' profile (Figure 7a & b). More edgewise compression increased overall axial compression (Figure 3b), agreeing with previous work [35,38–41,44]. A larger compressed volume for auxetic foam is expected, as shear modulus increases relative to Young's modulus while Poisson's ratio decreases from positive to negative values [12,67]. More overall deformation would increase energy absorption, supporting application of auxetic foam, and other auxetic materials, to protective equipment and cushioning [7,43,46,51,68–72]. The measured difference in the amount of compressed foam between auxetic and zero Poisson's ratio samples was largest during studded indentations (Figure 7b).

From the presented findings (Figure 5), auxetic foams ($\nu \approx -0.3$) should reduce penetration in quasi-static indentations (i.e., seating, bedding, climbing/gymnasium matts and packaging) [51,73]. Based on the theory (i.e., Equation 1 to 3), greater benefits are expected from higher magnitude NPR. Further work could now confirm the effects and the presence of increased indentation resistance, caused by (negative) Poisson's ratios, during impacts; which typically cause higher indentation depths (up to ~80% of sample thickness) and strain rates [46,70,71].

5. Conclusions

Calculated indentation force was typically within ~5% of the measured force. Close fit between calculations and experiment confirms that the NPR of auxetic foams increases

indentation resistance. The highest normalised indentation forces (F/E) were observed for the auxetic foams (with Poisson's ratios of -0.3). Digital image corelation and vector plots showed auxetic foam deformed as a flatter unit, meaning more foam was compressed, and exhibited more densification due to transverse contraction, than non-auxetic foams. Collected data provides empirical evidence to potential benefits of auxetic materials for impact protection, and robust validation of the underlying theoretical benefits.

Acknowledgements

The authors would like to thank Sheffield Hallam University for supplying the funding to carry out the work (via their Graduate Teaching Associate scholarship), and the expert reviewers for their comments that helped us to improve the manuscript.

Author Contributions

Dr Duncan conceptualised the study, undertook the experimental work and analysis, and wrote the manuscript. Drs Allen and Foster, and Prof Alderson, provided feedback throughout.

Data statement

Research data will be stored by the authors until 2026 and can be accessed upon reasonable request.

6. References

1. Roark RJ, Young WC. Formulas for stress and strain. McGraw-Hill, USA; **2012**. 20–22, 48–50 p.
2. Lakes RS. Foam Structures with a Negative Poisson's Ratio. Science (80-). 1987.235(4792). 1038–40.
3. Evans KE, Alderson A. Auxetic materials: Functional materials and structures from lateral thinking! Adv Mater. 2000.12(9). 617–28.
4. Kolken HMA, Zadpoor AA. Auxetic mechanical metamaterials. RSC Adv. 2017.7. 5111–29.
5. Ren X, Das R, Tran P, Ngo TD, Xie YM. Auxetic metamaterials and structures: a review. Smart Mater Struct. 2018.27. 023001.
6. Lakes RS. Negative-Poisson's-Ratio Materials: Auxetic Solids. Annu Rev Mater Res. 2017.47. 63–81.
7. Duncan O, Shepherd T, Moroney C, Foster L, Venkatraman PD, Winwood K, et al. Review of auxetic materials for sports applications: Expanding options in comfort and protection. Appl Sci. 2018.8(6). 941.
8. Lim TC. Auxetic Materials and Structures. Springer Singapore; **2015**.
9. Hu H, Zhang M, Yanping L. Auxetic Textiles. Woodhead Publishing Ltd.; **2019**.
10. Lim T-C. Mechanics of Metamaterials with Negative Parameters. Singapore: Springer Nature; **2020**.
11. Lakes RS. Composites and Metamaterials. World Scientific; **2020**.
12. Timoshenko SP, Goodier JN. Theory of Elasticity. 3rd ed. New York: McGraw-Hill, USA; **1970**.
13. Alderson KL, Pickles AP, Neale PJ, Evans KE. Auxetic polyethylene: The effect of a negative Poisson's ratio on hardness. Acta Metall Mater. 1994.42(7). 2261–6.
14. Hertz HR, Jones D., Schott G. Miscellaneous papers. Macmillan Co Ltd. 1896.92. 156–71.
15. Fischer-Cripps AC. Nanoindentation. 3rd ed. Springer; **2004**.
16. Yu W, Blanchard JP. An elastic-plastic indentation model and its solutions. J Mater Res. 1996.11(9). 2358–67.

17. Popov VL, Heß M, Willert E. Handbook of contact mechanics: Exact solutions of axisymmetric contact problems. Handbook of Contact Mechanics: Exact Solutions of Axisymmetric Contact Problems. **2019**. 7-10,12 p.
18. Johnson K. Contact Mechanics. Cambridge, UK: Cambridge University Press; **1985**.
19. Popov VL. Contact Mechanics and Friction. Berlin: Springer Berlin Heidelberg; **2010**. 19,62.
20. Argatov II. Asymptotic modeling of the impact of a spherical indenter on an elastic half-space. Int J Solids Struct. 2008.45(18–19). 5035–48.
21. Martz EO, Lee T, Lakes RS, Goel VK, Park JB. Re-entrant transformation methods in closed cell foams. Cell Polym. 1996.15(4). 229–49.
22. Fan D, Li M, Qiu J, Xing H, Jiang Z, Tang T. Novel Method for Preparing Auxetic Foam from Closed-Cell Polymer Foam Based on the Steam Penetration and Condensation Process. ACS Appl Mater Interfaces. 2018.10(26). 22669–22677.
23. Bianchi M, Scarpa F, Banse M, Smith CW. Novel generation of auxetic open cell foams for curved and arbitrary shapes. Acta Mater. 2011.59(2). 686–91.
24. Grima JN, Attard D, Gatt R. A novel process for the manufacture of auxetic foams and for the conversion of auxetic foam to conventional form (WO 2010049511 A2). 2010. 1–5.
25. Li Y, Zeng C. Room-Temperature, Near-Instantaneous Fabrication of Auxetic Materials with Constant Poisson's Ratio over Large Deformation. Adv Mater. 2016.28(14). 2822–6.
26. Critchley R, Corni I, Wharton JA, Walsh FC, Wood RJK, Stokes KR. A review of the manufacture, mechanical properties and potential applications of auxetic foams. Phys Status Solidi Basic Res. 2013.250(10). 1963–82.
27. Jiang W, Ren X, Wang SL, Zhang XG, Zhang XY, Luo C, et al. Manufacturing, characteristics and applications of auxetic foams: A state-of-the-art review. Compos Part B Eng. 2022.235. 109733.
28. Duncan O, Clegg F, Essa A, Bell AMT, Foster L, Allen T, et al. Effects of Heat Exposure and Volumetric Compression on Poisson's Ratios, Young's Moduli, and Polymeric Composition During Thermo-Mechanical Conversion of Auxetic Open Cell Polyurethane Foam. Phys Status Solidi. 2019.256(1800393). 1–12.
29. Chan N, Evans KE. Fabrication methods for auxetic foams. J Mater Sci. 1997.32. 5945–53.
30. Chan N, Evans KE. The mechanical properties of conventional and auxetic foams. Part I: compression and tension. J Cell Plast. 1999.35(2). 130–65.
31. Li Y, Zeng C. On the successful fabrication of auxetic polyurethane foams: Materials requirement, processing strategy and conversion mechanism. Polym (United Kingdom). 2016.87. 98–107.
32. Boba K, Bianchi M, McCombe G, Gatt R, Griffin AC, Richardson RM, et al. Blocked shape memory effect in negative Poisson's ratio polymer metamaterials. ACS Appl Mater Interfaces. 2016.8(31). 20319–20328.
33. Gibson LJ, Ashby MF. Cellular solids. Structure and properties. Cambridge: Press Syndicate of the University of Cambridge; **1997**. 4, 67, 103, 106, 167–169, 176–183, 259–264, 286, 3 p.
34. Allen T, Duncan O, Foster L, Senior T, Zampieri D, Edeh V, et al. Auxetic foam for snow-sport safety devices. In: Snow Sports Trauma and Safety. 1st ed. Cham, Switzerland: Springer; **2016**. p. 145–59.
35. Chan N, Evans KE. Indentation resilience of conventional and auxetic foams. J Cell Plast. 1998.34. 231–60.
36. Lakes RS, Elms K. Indentability of conventional and negative Poisson's ratio foams. J Compos Mater. 1993.27(12). 1193–202.
37. Alderson KL, Fitzgerald A, Evans KE. The strain dependent indentation resilience of auxetic microporous polyethylene. J Mater Sci. 2000.35(16). 4039–47.
38. Aw J, Zhao H, Norbury A, Li L, Rothwell G, Ren J. Effects of Poisson's ratio on the deformation of thin membrane structures under indentation. Phys Status Solidi Basic Res. 2015.252(7). 1526–32.
39. Argatov II, Sabina FJ. Small-scale indentation of an elastic coated half-space: The effect of compliant substrate. Int J Eng Sci. 2016.104. 87–96.
40. Morris DJ, Cook RF. Indentation fracture mechanics model. 2008.23(9). 2429–42.
41. Li S, Al-Badani K, Gu Y, Lake M, Li L, Rothwell G, et al. The Effects of Poisson's Ratio on the Indentation Behavior of Materials With Embedded System in an Elastic Matrix. Phys Status Solidi Basic Res. 2017.254(12). 1–8.
42. Photiou D, Sarris E, Constantinides G. On the conical indentation response of elastic auxetic materials: Effects of Poisson's ratio, contact friction and cone angle. Int J Solids Struct. 2016.81. 33–42.
43. Scarpa F, Giacomin J, Zhang Y, Pastorino P. Mechanical performance of auxetic polyurethane foam for antivibration glove applications. Cell Polym. 2005.24(5). 253–68.
44. Kumar N, Khaderi SN, Rao KT. Elasto-Plastic Indentation of Auxetic and Metal Foams. J Appl Mech. 2020.87(January). 1–7.
45. Novak N, Duncan O, Allen T, Alderson A, Vesenjak M, Ren Z. Shear modulus of conventional and auxetic open-cell foam. Mech Mater. 2021.257. 104743.
46. Allen T, Shepherd J, Hewage TAM, Senior T, Foster L, Alderson A. Low-kinetic energy impact response of auxetic and conventional open-cell polyurethane foams. Phys Status Solidi Basic Res. 2015.9. 1–9.
47. Critchley R, Smy V, Corni I, Wharton JA, Walsh FC, Robert JK, et al. Experimental and computation assessment of thermomechanical effects during auxetic foam fabrication. Sci Rep. 2020.10(18301).
48. Annual Book of ASTM Standards. Standard Test Methods for Flexible Cellular Materials — Slab, Bonded, and Molded Urethane Foams. Annual Book of ASTM Standards 2008.
49. Duncan O, Allen T, Foster L, Senior T, Alderson A. Fabrication, characterisation and modelling of uniform and gradient auxetic foam sheets. Acta Mater. 2017.126. 426–37.
50. Allen T, Hewage T, Newton-Mann C, Wang W, Duncan O, Alderson A. Fabrication of Auxetic Foam Sheets for Sports Applications. Phys Status Solidi Basic Res. 2017.1700596. 1–6.
51. Lowe A, Lakes RS. Negative Poisson's ratio foam as seat cushion material. Cell Polym. 2000.19(3). 157–67.

52. Chiang FP, Uzer G. Mapping full field deformation of auxetic foams using digital speckle photography. Phys Status Solidi Basic Res. 2008.245(11). 2391–4.
53. Phillips N, Hassan GM, Dyskin A, Macnish C, Pasternak E. Digital image correlation to analyze nonlinear elastic behavior of materials. Proc - Int Conf Image Process ICIP. 2018.2017-Septe.
54. Argatov II, Mishuris GS, Paukshto M V. Cylindrical lateral depth-sensing indentation testing of thin anisotropic elastic films. Eur J Mech / A Solids. 2015.49. 299–307.
55. Popov VL, Willert E, Heß M. Method of dimensionality reduction in contact mechanics and friction: A user's handbook. iii. viscoelastic contacts. Vol. 16, Facta Universitatis, Series: Mechanical Engineering. **2018**. 19 p.
56. Huber MT. The theory of crosswise reinforced ferroconcrete slabs and its application to various important constructional problems involving rectangular slabs. Der Bauingenieur. 1923.4(12). 354–60.
57. Li Y, Barbi J. Stable Orthotropic Materials. In: Proceedings of the ACM SIGGRAPH/Eurographics Symposium on Computer Animation Eurographics Association. **2014**. p. 41–6.
58. Chai T, Draxler RR. Root mean square error (RMSE) or mean absolute error (MAE)? -Arguments against avoiding RMSE in the literature. Geosci Model Dev. 2014.7(3). 1247–50.
59. Bland JM, Altman DG. Applying the right statistics : analyses of measurement studies. Ultrasound Obs Gynecol. 2003.22. 85–93.
60. Bland JM, Altman DG. Statistical methods for assessing agreement between two methods of clinical measurement. Lancet. 1968.327(8476). 307–10.
61. Stelman HJ. Chapter 6 The t-test and Basic Inference Principles. In: Experimental Design and Analysis. CMU Statistics; **2018**. p. 141–70.
62. Gatt R, Attard D, Manicaro E, Chetcuti E, Grima JN. On the effect of heat and solvent exposure on the microstructure properties of auxetic foams: A preliminary study. Phys Status Solidi Basic Res. 2011.248(1). 39–44.
63. Argatov II. Solution of the plane Hertz problem. J Appl Mech Tech Physic. 2001.42(6). 1064–72.
64. Lakes R, Drugan WJ. Bending of a Cosserat Elastic Bar of Square Cross Section: Theory and Experiment. J Appl Mech Trans ASME. 2015.82(9). 1–16.
65. Lim TC, Alderson A, Alderson KL. Experimental studies on the impact properties of auxetic materials. Phys Status Solidi. 2014.251(2). 307–13.
66. Shepherd T, Allen T, Winwood K, Venkatraman PD, Alderson A. Validation of a Finite Element Modelling Process for Auxetic Structures under Impact. Phys Status Solidi B Basic Solid State Phys. 2020.1900197.
67. Chan N, Evans KE. The Mechanical Properties of Conventional and Auxetic Foams. Part II: Shear. J Cell Plast. 1999.35. 166–83.
68. Stojmanovski Mercieca LA, Formosa C, Grima JN, Chockalingam N, Gatt R, Gatt A. On the Use of Auxetics in Footwear: Investigating the Effect of Padding and Padding Material on Forefoot Pressure in High Heels. Phys Status Solidi Basic Res. 2017.254(12). 1–5.
69. Duncan O, Foster L, Senior T, Alderson A, Allen T. Quasi-static characterisation and impact testing of auxetic foam for sports safety applications. Smart Mater Struct. 2016.25(5). 054014.
70. Ge C. A comparative study between felted and triaxial compressed polymer foams on cushion performance. J Cell Plast. 2013.49(6). 521–33.
71. Lisiecki J, Błazejewicz T, Kłysz S, Gmurczyk G, Reymer P, Mikułowski G. Tests of polyurethane foams with negative Poisson's ratio. Phys Status Solidi Basic Res. 2013.250(10). 1988–95.
72. Sanami M, Ravirala N, Alderson K, Alderson A. Auxetic materials for sports applications. Procedia Eng. 2014.72. 453–8.
73. Wang YC, Lakes R. Analytical parametric analysis of the contact problem of human buttocks and negative Poisson's ratio foam cushions. Int J Solids Struct. 2002.39(18). 4825–38.